Pergamon

Int. J. Heat Mass Transfer. Vol. 41, No. 11, pp. 1485–1497, 1998

Printed in Great Britain
0017-9310/98 $19.00+0.00

PII: S0017-9310(97)00239-1

Numerical and experimental study of swirling flow in a model combustor

J. L. XIA† and G. YADIGAROGLU
Nuclear Engineering Laboratory, Swiss Federal Institute of Technology, ETH-Zentrum, CLT, CH-8092 Zurich, Switzerland

Y. S. LIU and J. SCHMIDLI
Gas Turbine Development, ABB Power Generation Ltd, CH-5401 Baden, Switzerland

and

B. L. SMITH
Thermal Hydraulics Laboratory, Paul Scherrer Institute, CH-5232 Villigen PSI, Switzerland

(*Received* 17 *February* 1997 *and in final form* 21 *July* 1997)

Abstract—The present paper describes a numerical and experimental investigation of strongly swirling flow in a water model combustion chamber equipped with a swirler of special design. The turbulence models used for the numerical calculations are the standard k–ε model, the RNG k–ε model and a differential Reynolds stress model (DRSM). In the water model, local mean velocity components and normal stresses are measured using a laser Doppler anemometer. Comparison of numerical predictions against experimental data reveals the superiority of the DRSM over the standard and RNG k–ε models. The DRSM captures all the major features of the swirling flow, while the other two models do not. For instance, both the experimental data and the DRSM predictions reveal complex, interesting flow behaviour: a corner recirculation zone, and a central toroidal recirculation zone connected to a central reverse zone, which persists all the way to the outlet of the chamber. However, the other two turbulence models predict that the swirling flow evolves into a solid-body-rotation-type flow downstream. The RNG k–ε model gives very little improvement over the standard k–ε model for the swirling flow case considered.

1. INTRODUCTION

The configuration considered in the present paper is the water model of a combustion chamber, schematically illustrated in Fig. 1. The model is equipped with a specially-designed, multi-channel swirler to induce a strong swirling flow favourable to combustion. The main objective of this study is to clarify the characteristics of turbulent swirling flow occurring in the combustion chamber, and to evaluate the performance of three turbulence models in predicting turbulent swirling flow by comparison with the measured data obtained using a laser-Doppler anemometer.

In modern combustors, swirl is commonly used to produce high rates of entrainment and fast mixing and to enhance the flame stability. Traditionally, the designers have relied heavily on empirical correlations for determining overall geometries, dimensions, etc. This approach is now supplemented with theoretical and computational modelling techniques, which have the ability to predict physical phenomena over a wide range of conditions, in addition to providing a better insight into the fluid dynamics.

Despite the recent advances in turbulence modelling, unavailability of accurate and reliable turbulence closure models is still one of the main obstacles in modelling complex turbulent swirling flows. Most of studies performed have utilized the eddy-viscosity models of turbulence. Though the k–ε model (KEM)

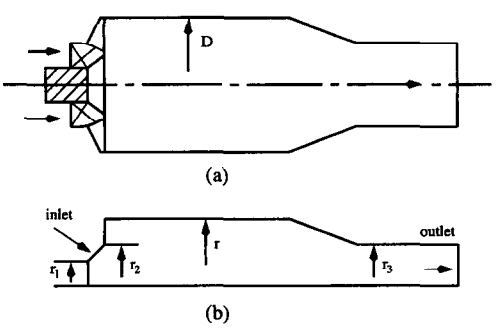

Fig. 1. Geometry of combustion chamber: (a) physical; (b) numerical.

† Permanent address: Institute of Engineering Thermophysics, Chongqing University, Chongqing 630044, China.

NOMENCLATURE

C	empirical constants in the turbulence model
D	chamber diameter
d_{ijk}	diffusion term in the turbulence model
k	turbulence kinetic energy
N_r	radial number
P_{ij}	production term of $\overline{u_i u_j}$
r	radius
Re	Reynolds number
S	swirl number
u_i	velocity fluctuation in the x_i-direction
$\overline{u_i u_j}$	Reynolds stresses
U	mean axial velocity
U_i	mean velocity in the x_i-direction
V	mean radial velocity
W	mean tangential velocity
x_i	spatial coordinate in the i-direction.

Greek symbols

β	constant in the RNG k–ε model
δ_{ij}	Kronecker delta
ε	dissipation rate of k
η_0	constant in the RNG k–ε model
μ	dynamic viscosity
μ_t	turbulent viscosity
ν	kinematic viscosity
ρ	fluid density
σ	empirical diffusion coefficients in the turbulence model
φ_{ij}	pressure-strain term in the turbulence model.

Subscripts

i, j	spatial coordinates.

performs well for simple flow cases [1], it has been found less satisfactory for swirling flows and poorly predicts the size and strength of recirculation zones [2–4]. The KEM tends to produce an excessive solid-body component type of rotation for swirling flows, probably due to the isotropic eddy viscosity assumption; it is known that the turbulence is highly anisotropic in swirling flows [5]. The Renormalization Group Theory (RNG) of Yakhot *et al.* [6] appears to offer new theoretical support to the basic form of the ε equation, and to take better account of the effects of extra strain rates [7]. Though the RNG KEM can produce results superior to the standard KEM for separated flows and flows with high streamline curvature and strain rate [6], Lai [8] showed that it failed to capture the key features of swirling flow with swirl number $S = 0.5$.

Attempts have also been made to include anisotropic effects into turbulence models. A simple method of closure is to introduce algebraic relations for the Reynolds stresses in the differential transport equations [9]: the algebraic Reynolds stress model (ARSM). Benim [10] used the ARSM to model turbulent swirling flows and found that it could produce significantly more accurate results than the standard KEM. However, the evidence is not conclusive, and Fu *et al.* [11] maintain that the ARSM is unsatisfactory for swirling flows.

One of the most complex levels of turbulence closure is the differential Reynolds stress model (DRSM) which solves the Reynolds stresses from their respective transport equations. Few studies have been made using the DRSM to predict swirling flows. Jones and Pascau [12] and Hogg and Leschziner [13] applied the DRSM to a confined, swirling flow with non-swirling central jet and found that the predicted mean velocity profiles were in good agreement with the experimental data of So *et al.* [14]. Ohtsuka [15] predicted swirling, non-reacting and reacting flows using the DRSM and pointed out that the intensity of the axial and swirl velocities near the centreline was underestimated. Other studies include, for example, the work by Sharif and Wong [16], who carried out a comparative investigation of a nonlinear k–ε model, a DRSM and an ARSM in predicting confined swirling flows and by Zhu and Shih [17] who examined the predictive capability of a RNG KEM and a realizable Reynolds stress model for confined co-flowing jets.

The present study investigates the swirling flow characteristics occurring in a water model combustion chamber and the predictive capabilities of the standard KEM, a RNG KEM and a DRSM for strongly swirling flow. Predictions are compared with experimental data obtained using a laser Doppler anemometer (LDA). Such comparison is necessary to evaluate the numerical solutions. In contrast to previous studies, which have used experimental data or assumed velocity profiles to provide the inlet boundary conditions, those for the present numerical calculations are derived from a three-dimensional simulation of flow in the swirler channels [18]. Further, and again contrasting earlier studies, the inlet is oblique to the chamber axis, and a contraction region is also included towards the outlet, as shown in Fig. 1.

2. EXPERIMENTAL DETAILS

The geometry of the model combustion chamber is displayed schematically in Fig. 1(a) and the layout of

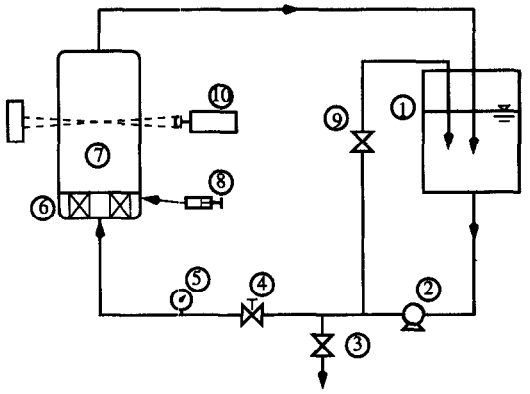

Fig. 2. Experimental set-up: (1) water tank; (2) centrifugal pump; (3) drain pipe; (4) flow adjusting valve; (5) flowmeter; (6) swirler; (7) tested combustion chamber model; (8) dye injection; (9) by-pass; (10) laser Doppler anemometer.

the experimental set-up is sketched in Fig. 2. The working fluid is tap water with pressure slightly higher than 1 bar. The chamber is a cylindrical tube, 288 mm inner diameter and 1200 mm axial length, with a contraction region in front of the chamber exit. The transparent plexiglass wall, which has nearly the same refractivity as water, allows flow visualization and access of LDA beams. A multi-channel swirler having a special design of engineering interest is installed at the chamber inlet to induce swirling. The mass flowrate is 9.5 kg/s, corresponding to an inlet Reynolds number based on chamber diameter $Re = 2.19 \times 10^5$.

In addition to the measurement of water flowrate by means of an inductive flowmeter, the mean velocity components (axial, radial and tangential velocities) and the normal Reynolds stress distributions at various axial planes are measured using a standard two-component laser Doppler anemometer working in a backward scattering mode. The optical components of the anemometer consist of a 5 W Argon ion laser, a rotating diffraction, a light-collection arrangement, a photomultiplier and a signal processing system. It is known that this instrumentation allows the measurement of mean velocity components and the r.m.s. of the corresponding fluctuations with very high precision. The measured data are read in a computer-auxiliary acquisition system. In order to minimize errors induced by refraction at the curved cylindrical wall, the chamber is placed in a rectangular water jacket to allow nearly perpendicular access of the LDA beams. Because the refractive indices of plexiglass/water arrangements are much closer than those of air/plexiglass, errors induced by curvature at the cylinder wall are reduced. The volume flowrate obtained from the velocity profiles measured using LDA was cross-checked against that from the flowmeter. The comparison indicates uncertainties in the mean velocity measurements of $\pm 5\%$. It is very difficult to give similar estimates for the errors in the Reynolds stress measurements. Other authors, e.g. Imao and Itoh [19], claim about 10% for the LDA set-up used here.

The LDA measurements are made at numerous radial locations at seven axial positions ($x/D = 0.2$, 0.406, 0.615, 1.267, 1.441, 1.615 and 2.448).

3. MATHEMATICAL MODEL

3.1. *Governing equations*

Steady-state, incompressible, turbulent flows are governed by the Reynolds-averaged continuity and Navier–Stokes equations. The conservative forms of these equations in tensor notation can be written as

$$\frac{\partial(\rho U_j)}{\partial x_j} = 0; \tag{1}$$

$$\frac{\delta(\rho U_i U_j)}{\partial x_j} = -\frac{\partial P}{\partial x_i} + \frac{\partial}{\partial x_j}\left[\mu \frac{\partial U_i}{\partial x_j} - \rho\overline{u_i u_j}\right] \tag{2}$$

where ρ is the (constant) density, x_j the coordinate, μ the dynamic viscosity, and U_j and u_j are, respectively, the mean and the corresponding fluctuation velocity components in the j direction.

The numerical solution of the above set of mean equations is obtained by introducing additional transport equations for the Reynolds stresses $\rho\overline{u_i u_j}$. These equations contain higher-order correlations which represent the processes of diffusion transport, viscous dissipation and fluctuating pressure-velocity interactions and have to be approximated by model assumptions in order to close the system of equations. The Reynolds stresses are calculated here by using one of the following three turbulence models.

Standard k–ε *model, KEM.* The Reynolds stress term is assumed, at high turbulent Reynolds number [1], to be of the form

$$-\rho\overline{u_i u_j} = 2\mu_t S_{ij} - \tfrac{2}{3}\rho k \delta_{ij}, \tag{3}$$

where

$$S_{ij} = \frac{1}{2}\left(\frac{\partial U_i}{\partial x_j} + \frac{\partial U_j}{\partial x_i}\right) \tag{4}$$

is the mean rate-of-strain tensor. The eddy viscosity is given by:

$$\mu_t = C_\mu \rho \frac{k^2}{\varepsilon} \tag{5}$$

in which

$$k = \tfrac{1}{2}\overline{u_i u_i}; \quad \varepsilon = \nu\overline{\frac{\partial u_i}{\partial x_j}\frac{\partial u_i}{\partial x_j}} \tag{6}$$

are the turbulent kinetic energy and dissipation rate, respectively. These satisfy the following transport equations at each point of the flow domain:

Table 1. Values of constants for eddy-viscosity models

	C_μ	$C_{\varepsilon 1}$	$C_{\varepsilon 2}$	σ_k	σ_ε
KEM	0.09	1.44	1.92	1.0	1.3
RNG KEM	0.085	$1.42-\frac{\eta\left(1-\frac{\eta}{\eta_0}\right)}{1+\beta\eta^3}$	1.68	0.7179	0.7179

$$\frac{\partial(\rho U_j k)}{\partial x_j}=\frac{\partial}{\partial x_j}\left[\left(\mu+\frac{\mu_t}{\sigma_k}\right)\frac{\partial k}{\partial x_j}\right]+2\mu_t S_{ij}S_{ij}-\rho\varepsilon; \tag{7}$$

$$\frac{\partial(\rho U_j \varepsilon)}{\partial x_j}=\frac{\partial}{\partial x_j}\left[\left(\mu+\frac{\mu_t}{\sigma_\varepsilon}\right)\frac{\partial \varepsilon}{\partial x_j}\right]+2C_{\varepsilon 1}\frac{\varepsilon}{k}\mu_t S_{ij}S_{ij}-C_{\varepsilon 2}\rho\frac{\varepsilon^2}{k}. \tag{8}$$

The model transport equations contain five coefficients: C_μ, $C_{\varepsilon 1}$, $C_{\varepsilon 2}$, σ_k and σ_ε. In the standard KEM, these coefficients have been obtained from benchmark experiments for equilibrium turbulent boundary layers and isotropic turbulence, and are shown in the first row of Table 1.

RNG k–ε *model.* The RNG k–ε model [6] is of the same form as the standard KEM except for the specification of the model coefficients listed in the second row of Table 1, in which $\eta=(k/\varepsilon)(2S_{ij}S_{ij})^{1/2}$, $\eta_0=4.38$ and $\beta=0.015$.

Differential Reynolds stress model, DRSM. In the DRSM, the Reynolds stresses are calculated from their own transport equations and the concept of an (isotropic) eddy viscosity is no longer required. The model assumptions used in the present study are described in detail by Clarke and Wilkes [20] and are outlined as follows.

$$\frac{\partial(\rho U_k\overline{u_iu_j})}{\partial x_k}=\rho(P_{ij}-\varepsilon_{ij}+\varphi_{ji}+d_{ijk}) \tag{9}$$

where

$$P_{ij}=-\left[\overline{u_ju_k}\frac{\partial U_i}{\partial x_k}+\overline{u_iu_k}\frac{\partial U_j}{\partial x_k}\right] \tag{10}$$

$$d_{ijk}=C_s\frac{\partial}{\partial x_k}\left(\frac{k}{\varepsilon}\overline{u_ku_l}\frac{\partial\overline{u_iu_j}}{\partial x_l}\right) \tag{11}$$

$$\varphi_{ij}=-C_1\frac{\varepsilon}{k}\left(\overline{u_iu_j}-\frac{2}{3}\delta_{ij}k\right)-C_2\left(P_{ij}-\frac{1}{3}\delta_{ij}P_{kk}\right) \tag{12}$$

$$\varepsilon_{ij}=2\nu\overline{\frac{\partial u_i}{\partial x_k}\frac{\partial u_j}{\partial x_k}}=\frac{2}{3}\delta_{ij}\varepsilon. \tag{13}$$

Table 2. Values of model constants for DRSM

C_1	C_2	C_ε	C_s	$C_{\varepsilon,1}$	$C_{\varepsilon,2}$
1.8	0.6	0.22	0.16	1.44	1.92

The turbulent energy dissipation rate is calculated from the following modelled transport equation:

$$\frac{\partial(U_k\varepsilon)}{\partial x_k}=C_\varepsilon\frac{\partial}{\partial x_k}\left(\frac{k}{\varepsilon}\overline{u_ku_l}\frac{\partial\varepsilon}{\partial x_l}\right)+\frac{1}{2}C_{\varepsilon,1}\frac{\varepsilon}{k}P_{kk}-C_{\varepsilon,2}\frac{\varepsilon^2}{k} \tag{14}$$

with k given in equation (6). The values of the constants utilized in the model are shown in Table 2.

3.2. *Geometry and boundary conditions*

The flow configuration considered in the numerical simulation is based on the water model of the combustion chamber used in the experiment; 2-D axisymmetry is assumed (see Fig. 1). The chamber radius $r=0.144$ m, with an inlet which is oblique to the axis, extending from $r_1=0.03$ m to $r_2=0.07$ m. The contraction region is from $x/D=1.84$ to $x/D=2.326$, with the radius at the chamber outlet $r_3=0.095$ m. The physical outlet of the combustion chamber is located at $x/D=2.45$, where x is the axial length and D is the chamber diameter. Since it has been shown by Xia *et al.* [18] that the outlet boundary conditions have some influence on the flow upstream locally near the outlet, the computational domain has been extended to $x/D=4.17$ in order to avoid the effect of the presumed outlet boundary conditions. A constant mass flow rate boundary condition is imposed at the outlet, as derived from the inlet mass flow rate, and normal gradients are set to zero for all flow variables.

In contrast to the previous studies, which either used measured profiles or assumed constant profiles, frequently with zero radial velocity component, the inlet velocity profiles in the present simulation are derived from the 3-D calculation of turbulent flow inside a multi-channel swirler, results of which were partly reported by Xia *et al.* [18]. The swirl number S and the radial number N_r at the inlet are

$$S = \frac{\int_{r_1}^{r_2} 2\pi\rho UWr^2\,\mathrm{d}r}{r_2\int_{r_1}^{r_2} 2\pi\rho U^2 r\,\mathrm{d}r} = 1.68,$$

$$N_r = \frac{\int_{r_1}^{r_2} 2\pi\rho UVr\,\mathrm{d}r}{\int_{r_1}^{r_2} 2\pi\rho U^2 r\,\mathrm{d}r} = 0.697, \qquad (15)$$

in which U, V and W are the mean axial, radial and tangential velocity components. The radial number N_r was introduced by Xia *et al.* [18] and shown to have a strong influence on the characteristics of swirling flow. The turbulent kinetic energy k and its dissipation rate ε at the inlet are chosen as

$$k = 0.002V_{\text{in}}^2, \quad \varepsilon = \frac{k^{3/2}}{0.3l} \qquad (16)$$

where $V_{\text{in}} = \sqrt{U^2 + V^2 + W^2}$ is the total inlet velocity and l the length of the slope at the inlet. The turbulent normal stresses $\overline{uu}$, $\overline{vv}$ and $\overline{ww}$ are assumed to be equal and all the shear stresses are set to zero. At the centreline, the radial derivatives of all quantities are set to zero. Additionally, W, $\overline{uv}$ and $\overline{vw}$ are set to zero due to symmetry.

3.3. *Solution procedure*

The mean flow and turbulence transport equations are solved numerically using the CFX-F3D code [21], which is a general-purpose solver for heat transfer and fluid flow in complex geometries and has been extensively validated against experimental data for many flow cases. A finite-volume, non-staggered grid approach is used. A QUICK scheme [22] is applied for the space derivatives of the advection terms in all transport equations. The pressure–velocity coupling is resolved using the SIMPLEC algorithm [23]. Convergence of the solution is assumed when the sum of the normalized residuals for each conservation equation is reduced to about 10^{-5} and all variables at selected observation points in the flow domain remain unchanged within a certain number of iterations. It is found that the CPU time using the DRSM is about 2.7 times greater than that for the KEM within a single iteration and that the solution scheme is much less robust. Often, excessive under-relaxation must be applied in order to obtain convergence, with associated penalties in terms of total calculation times.

A 120×61 non-uniform mesh in the axial and radial directions was used, with the axial meshes clustered near the inlet and the contraction region. Further mesh refinement produced insignificant changes in the solutions.

4. RESULTS AND DISCUSSION

4.1. *Flow patterns*

Velocity vectors calculated using the three turbulence models are shown in Fig. 3 and the zero-axial-velocity contours in Fig. 4. The DRSM reveals, as can be seen from Figs. 3(a) and 4(a), that a corner recirculation zone (CRZ) appears just behind the expansion region, and there exists a central toroidal recirculation zone (CTRZ) which is connected with a central reverse zone (CeRZ). For the special model combustor used, the CeRZ extends all the way to the outlet of the combustion chamber, and maintains nearly the same radial extent along its entire length. The contraction does not affect the size of the CeRZ, even though the fluid accelerates in that region, indicating that the swirling motion dominates the flow behaviour. A small eddy near the centreline within $x/D < 0.23$ is also predicted. The same complex flow pattern depicted in Fig. 3(a) was observed in the experiment by flow visualizations recorded using a video camera (not shown here), and was also confirmed from the velocity field measurements taken by the laser Doppler anemometer, as will be seen later. Not only the shapes, but also the sizes, of all recirculation zones are correctly predicted by the DRSM: the calculated CRZ covers the distance from $x/D = 0.118$ to $x/D = 0.432$ and the CTRZ front plane is located at $x/D = 0.972$. At the physical exit of the chamber ($x/D = 2.45$) the CeRZ occupies the region $r/D = 0.076$ in the measurements while $r/D = 0.079$ is predicted by the DRSM.

In contrast, both the KEM and the RNG KEM do not reveal the existence of the CeRZ, although the RNG KEM provides a slightly improved prediction of the CTRZ over the KEM. The KEM predicts the smallest CTRZ volume. The failure of the two-equation turbulence models to predict the sizes and shapes of the recirculation zones may result from the isotropic eddy viscosity assumption and improperly accounting for the interaction between swirl and turbulence. It is noted that a narrow separation zone near the wall in front of the contraction region is predicted by both the KEM and the RNG KEM, while the DRSM does not predict this phenomenon.

The mean axial velocity distributions along the centreline of the chamber are displayed in Fig. 5. The DRSM predicts a central negative axial velocity after $x/D = 0.23$ and this negative velocity remains nearly constant for $x/D > 0.8$, indicating almost uniform strength of the CeRZ in that region. Also, the radial size of the CeRZ changes very little downstream, all the way to the chamber exit, as can be seen in Fig. 4(a). It is seen that the KEM produces a larger reverse flow velocity and a smaller CTRZ volume than the RNG KEM. Both the KEM and the RNG KEM fail to predict the existence of the central reversed flow downstream. This appears to be mainly due to improper representation of the interaction between swirl and turbulence by the eddy viscosity models.

4.2. *Mean velocities*

Comparisons between the calculated and measured radial distributions of the mean axial, radial and tan-

gential velocity components are shown in Fig. 6 at eight axial locations. The last two at $x/D = 2.448$ and $x/D = 4.167$, correspond to the physical chamber exit and the numerical outlet, respectively. The DRSM produces realistically the major features of the swirling flow. For the axial velocity, intricate radial profiles exist near the inlet region, and the mean velocity profiles (not only the shapes but also the magnitudes) predicted by the DRSM are in excellent agreement with the experimental data. At $x/D = 0.2$, there appear two negative-velocity regions, indicating the existence of the CRZ and the CTRZ. The local maximum of the axial velocity is located at $x/D = 0.18$ according to both the DRSM calculation and the measured data. At $x/D = 0.406$, there are three negative axial velocity regions, indicating that the CRZ, the CTRZ and the CeRZ exist at this location, and two local maxima: the one closer to the wall corresponds to that seen already at $x/D = 0.2$, approaching the wall with increasing axial distance. The other peak is located between the CTRZ and the CeRZ and this gradually moves away from the centreline, downstream. At $x/D = 0.615$, the CRZ diminishes, with the second maximum of the axial velocity approaching the wall. Further downstream, there exists one local maximum and the CeRZ persists up to the chamber outlet, as remarked earlier. The KEM and RNG KEM give reasonable axial velocity profiles only near the inlet region but, further downstream, totally fail to reproduce the CeRZ.

For the radical velocity, comparison with the experimental data is made for three axial planes near the inlet, where the radial effects are strongest. The radial velocity component decays rapidly and approaches zero after $x/D \approx 0.605$, according to both prediction and measurement. It is seen that all three turbulence models give reasonable radial velocity profiles. It has been shown by Xia *et al.* [18] that, although the radial velocity component decays very rapidly to zero, it is important to prescribe a realistic inlet radial velocity in order to obtain an accurate prediction of swirling flows; its effect may be estimated by the radial number N_r, defined in equation (15).

For the tangential velocity, the DRSM predicts a complex, combined free-forced vortex flow that persists all the way to the exit of the combustion chamber, again in excellent agreement with the measured profiles. The position of maximum tangential velocity moves towards the wall and this behaviour is well predicted by the DRSM. Near the inlet, two local maxima occur; these are also well predicted. Within the central region, the tangential velocity is somewhat underpredicted.

In summary, Fig. 6 shows that the DRSM predicted profile shapes for the mean axial, radial and tangential velocity components agree well with the data, their magnitudes are reasonably consistent, though there is a slightly larger discrepancy near the inlet, and again in the central region. The extremities of all the recirculation zones (CRZ, CTRZ and CeRZ) are correctly predicted by the DRSM. In contrast, both the KEM and the RNG KEM predict that the swirling flow eventually evolves to a solid-body-rotation-type, except near the wall. These results indicate that the DRSM is able to account for the interaction between swirl and turbulence and to reproduce the combined free-forced vortex character of the swirling flow. In contrast, the two eddy-viscosity models do not capture this interesting phenomenon, and overpredict the solid-body-rotation-type component for swirling flow.

4.3. *Turbulent quantities*

Figure 7 displays the radial dependence of the normal and shear Reynolds stresses at various axial locations. Measurements exist only for the normal stresses, represented by the r.m.s. values. As can be seen from the figure, the agreement between the DRSM prediction and the measured data is fairly good downstream of $x/D \approx 0.6$, especially for $x/D > 1.2$ where the predicted r.m.s. values, representing the intensities of turbulent fluctuations, are close to the measured data. It appears that the prediction is less satisfactory within the inlet region and the DRSM prediction for the normal stresses underestimates measured values near the centreline, which may be partially due to the flow field complexity and experimental uncertainty. It is seen that the most complex part of the flow occurs in the region of the inlet, where the turbulent normal and shear stresses vary intricately in the radial direction due to the interaction between CRZ, CTRZ and CeRZ. The level of anisotropy within the inlet region is quite marked, while beyond $x/D \approx 0.6$ the anisotropy revealed by both the DRSM and the experiment is not so obvious; that is, isotropic turbulence prevails downstream. Although measurements of the shear stresses are not available, their predicted values are also plotted in Fig. 7. The shear stresses are quite small, especially away from the inlet-region, which may be caused by the stabilizing effect of the swirling mean motion.

Finally, turbulent kinetic energy profiles for each of the three turbulence models are given in Fig. 8. We have seen in Fig. 7 that the r.m.s. values from the DRSM are close to the experimental data, where these exist. We therefore assume that the turbulent kinetic energy is correctly predicted by the DRSM and critically discuss the other models. It is seen from Fig. 8 that, near the inlet region, the RNG KEM prediction is closer to that of the DRSM while the KEM reveals much too high turbulent kinetic energy levels. Further downstream, the RNG KEM predicts higher kinetic energy. Approaching the exit of the combustion chamber, the two eddy viscosity models give similar values. Generally, the predicted turbulent kinetic energy by the two eddy-viscosity models is much too large, compared with the DRSM solutions. The RNG KEM appears to give some improvement of prediction near the inlet over the KEM.

(a) *DRSM*

(b) *RNG KEM*

(c) *KEM*

Fig. 3. Axial velocity vector plots: (a) DRSM; (b) RNG KEM; (c) KEM.

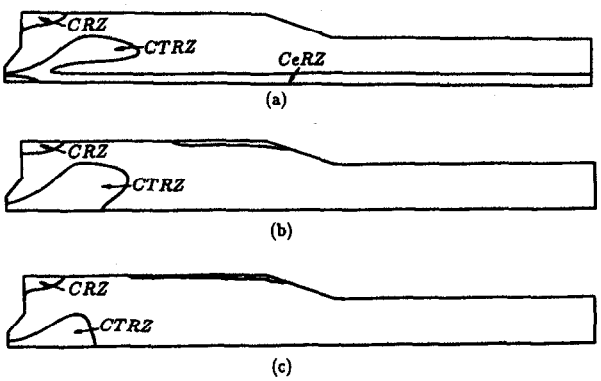

Fig. 4. Contours of zero-axial velocity: (a) DRSM; (b) RNG KEM; (c) KEM.

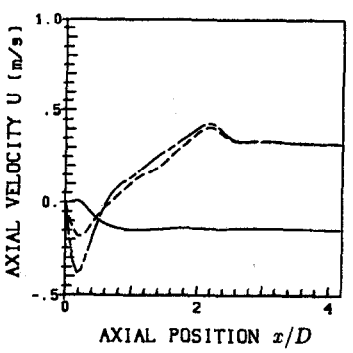

Fig. 5. Mean axial velocity distributions along the centreline: — DRSM; --- RNG KEM; ---- KEM.

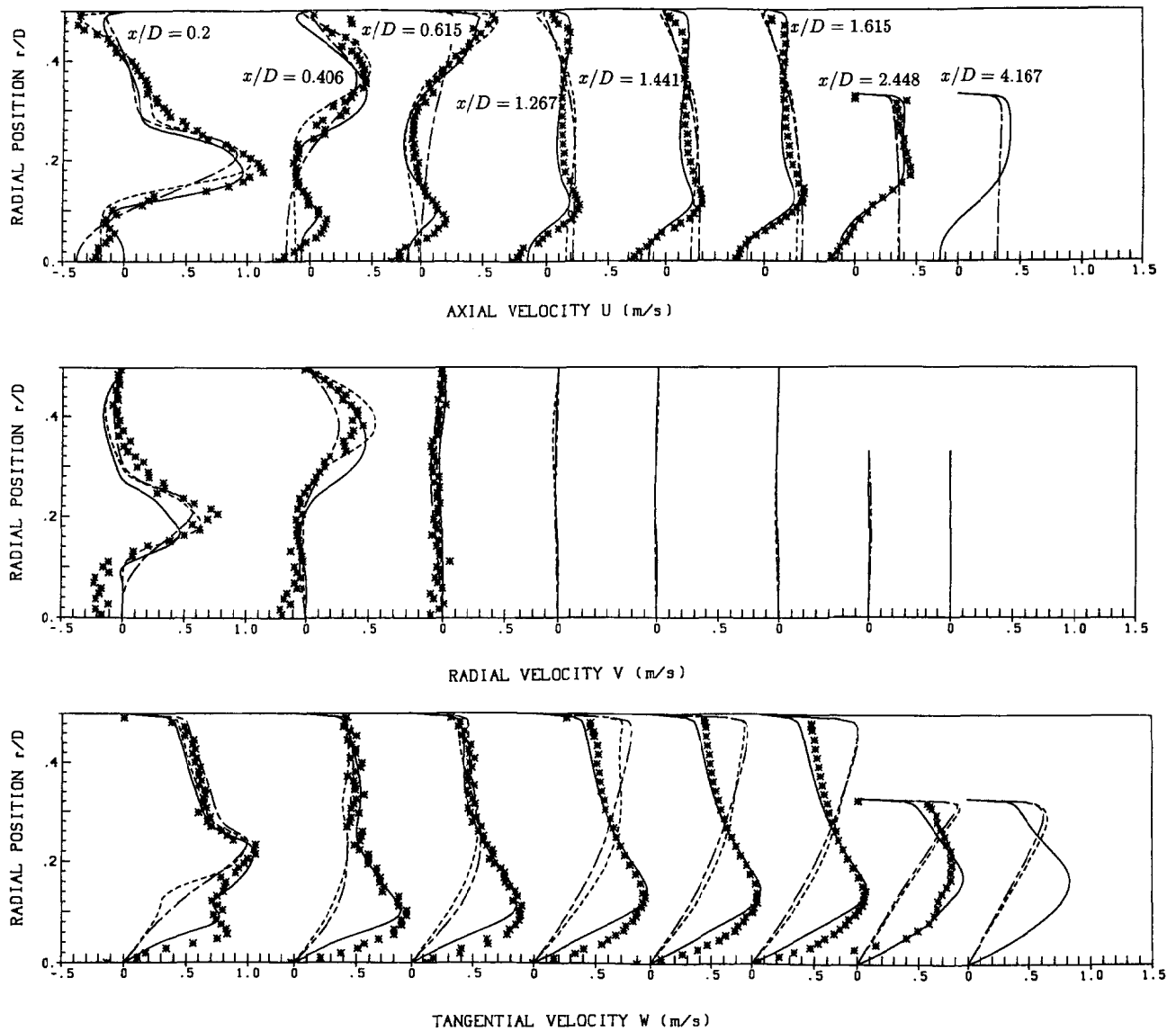

Fig. 6. Mean velocity profiles at various axial sections: * experimental; — DRSM; --- RNG KEM; – – – KEM.

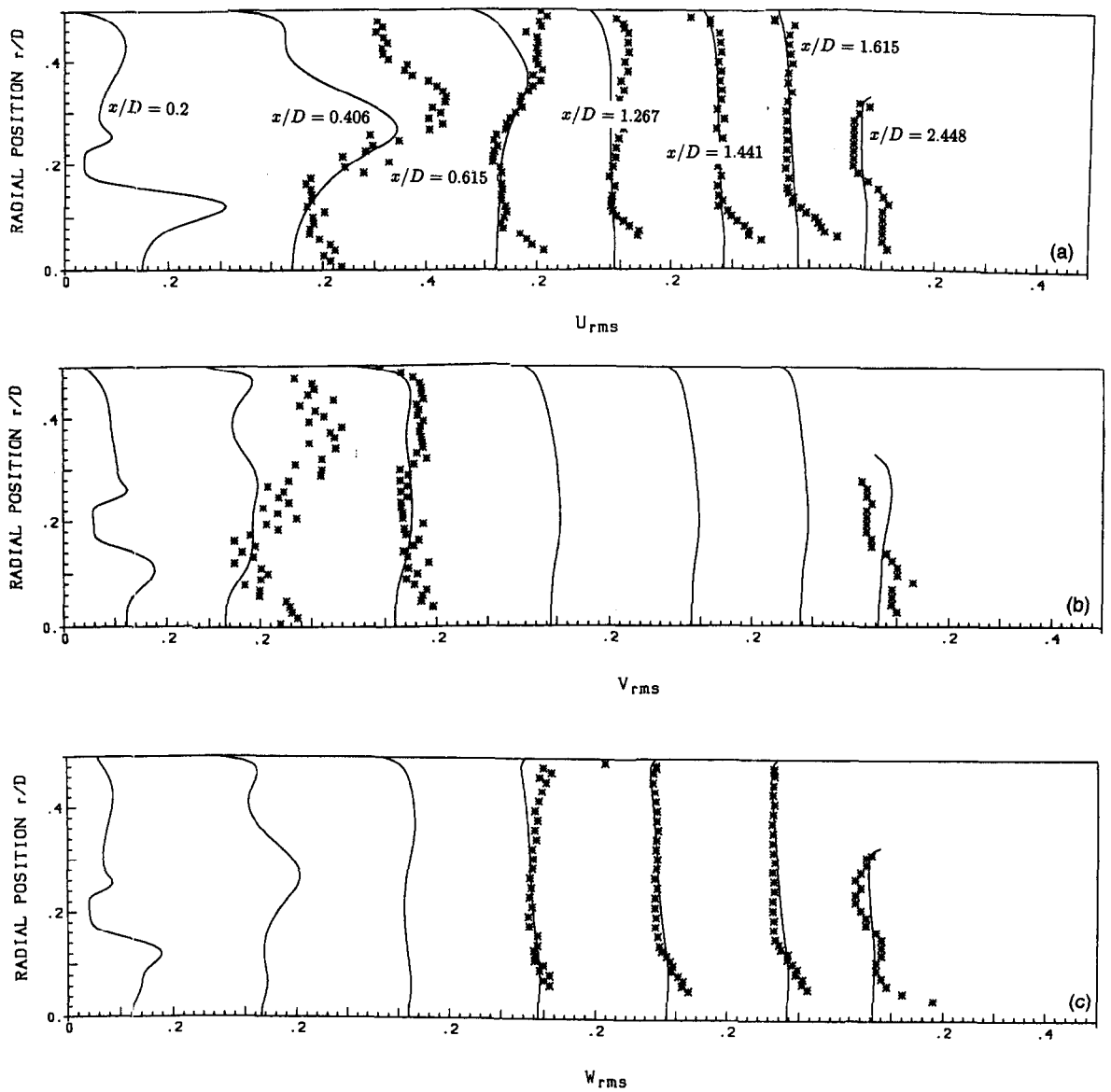

Fig. 7. Reynolds stress distributions at various axial sections: * experimental; — DRSM.

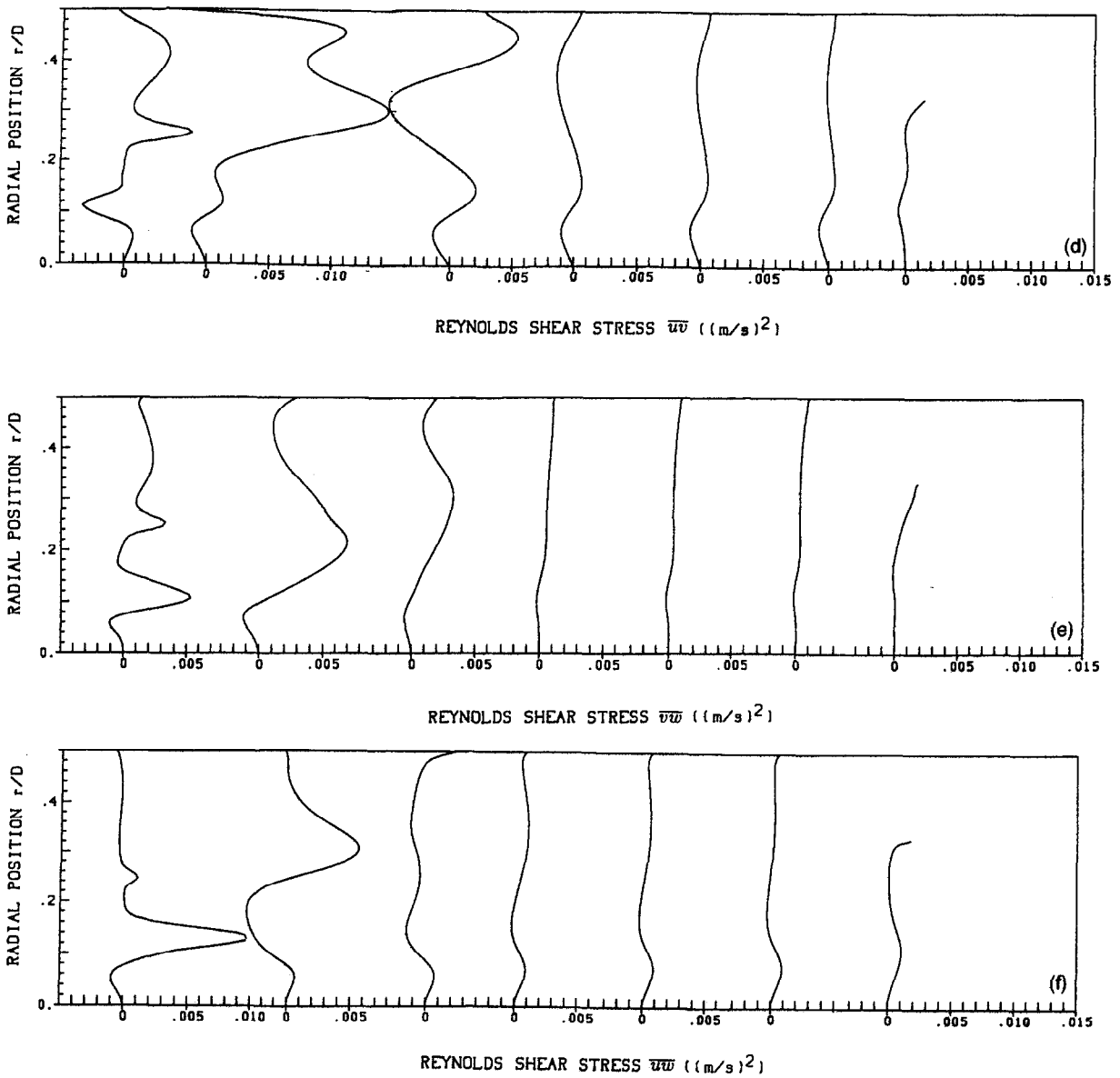

Fig. 7—*continued.*

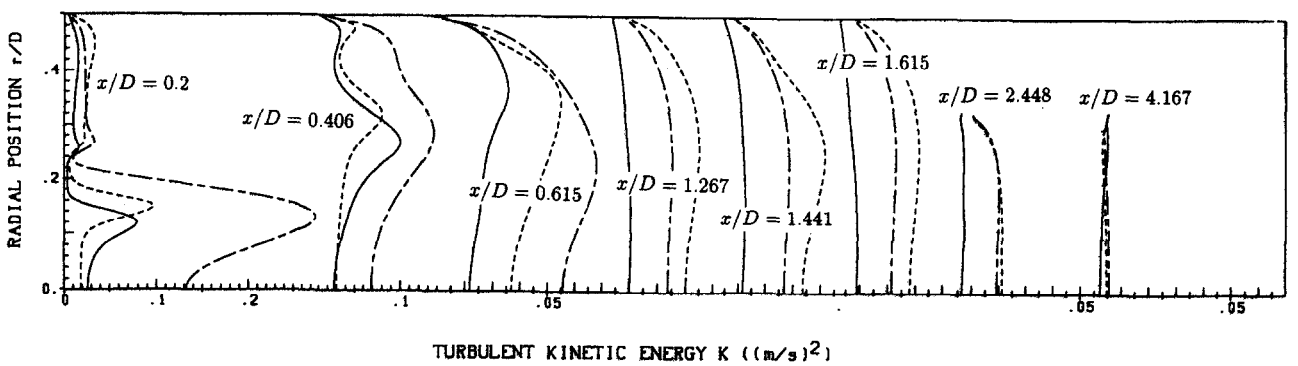

Fig. 8. Comparison of turbulent kinetic energy profiles; — DRSM; --- RNG KEM; – – – KEM.

5. CONCLUSIONS

Numerical and experimental investigations have been conducted for swirling flow occurring in a water model of a combustion chamber with a swirler of special design. Both the DRSM prediction and the experiment reveal a corner recirculation zone and a central toroidal recirculation zone, connected to a central reverse zone which extends all the way to the exit of the combustion chamber and remains nearly unchanged in its size and strength downstream. The swirling flow remains of a complex free-forced vortex type and does not evolve to a solid-body-rotation flow through the chamber.

The DRSM can reasonably predict the shapes and the sizes of all the recirculation zones, the mean velocity component profiles and the Reynolds stresses, although the prediction is less satisfactory near the centreline and near the inlet region. It is found that the level of the anisotropy within the inlet region is quite marked, while at $x/D > 0.6$, the turbulence is closely isotropic. The KEM and the RNG KEM do not predict the central reverse zone, although the RNG KEM appears to give some improvement of prediction near the inlet. The two eddy-viscosity models give reasonable prediction of the mean radial velocity component profile but not at all for the mean axial and tangential velocity component profiles, and grossly overpredict the turbulent kinetic energy levels. The main reason for the failure of the two eddy-viscosity models to adequately represent the swirling flow field is that they do not properly account for the interaction between swirl and turbulence.

The present study, though carried out under isothermal conditions with water, is relevant to the modelling of real combustion flows in combustors. Indeed in another paper [24], we discuss the similarities between the isothermal and combustion flows in similar geometry for the water tests described here. Comparisons of the experimental data to the associated numerical simulations validate the modelling for the isothermal case. As a consequence of the analysis performed in the present paper, we can approach the problem of modelling real combustion flows with increased confidence.

REFERENCES

1. Launder, B. E. and Spalding, D. B., The numerical computation of turbulent flows. *Comp. Meth. Appl. Mech. Engng*, 1974, **3**, 269.
2. Sloan, D. G., Smith, P. J. and Smoot, L. D., Modeling of swirl in turbulent flow systems. *Prog. Energy Combust. Sci.*, 1986, **12**, 163.
3. Sturgess, G. J. and Syed, S. A., Calculation of confined swirling flows. *AIAA Paper*, 85-0060, 1985.
4. Srinivasan, R. and Moagia, H. C., Numerical computation of swirling recirculating flow. *NASA CR* 165197, 1980.
5. Lilley, D. G. and Chigier, N. A., Nonisotropic turbulent stress distribution in swirling flows from mean value distribution. *Int. J. Heat Mass Transfer*, 1971, **14**, 573.
6. Yakhot, V., Orszag, S. A., Thangam, S., Gatski, T. B. and Speziale, C. G., Development of turbulence model for shear flows by double expansion technique. *Phys. Fluids*, 1992, **4**(7), 1510.
7. Hanjalic, K., Advanced turbulence closure models, a view of current status and future prospects. *Int. J. Heat and Fluid Flow*, 1994, **15**(3), 178.
8. Lai, Y. G., Predictive capabilities of turbulence models for a confined swirling flow. *FED*, 1994, **203**, 93.
9. Rodi, W., A new algebraic relation for calculating the Reynolds stresses. *ZAMM (Mech. Fluid)*, 1971, **56**, 219.
10. Benim, A. C., Finite element analysis of confined turbulent swirling flows. *Int. J. Numer. Methods Fluids*, 1990, **11**, 697.
11. Fu, S., Huang, P. G., Launder, B. E. and Leschziner, M. A., A comparison of algebraic and differential second-moment closure for axisymmetric turbulent shear flows with and without swirl. *ASME J. Fluids Eng.*, 1988, **110**, 216.
12. Jones, W. P. and Pascau, A., Calculation of confined swirling flows with a second moment closure. *J. Fluids Eng.*, 1989, **111**, 248.
13. Hogg, S. I. and Leschziner, M. A., Computation of highly swirling confined flow with a Reynolds stress turbulence model. *AIAA J.*, 1989, **27**, 57.
14. So, R. M. C., Ahmed, S. A. and Mongia, H. C., An experimental investigation of gas jets in confined swirling air flow. *NASA CR*-3832, 1984.
15. Ohtsuka, M., Numerical analysis of swirling nonreacting and reacting flows by the Reynolds stress differential method. *Int. J. Heat Mass Transfer*, 1995, **38**(2), 331.
16. Sharif, M. A. R. and Wong, Y. E., Evaluation of the performance of three turbulence closure models in the prediction of confined swirling flows. *Computers and Fluids*, 1995, **24**(1), 81.
17. Zhu, J. and Shih, T. H., Computation of confined coflow jets with three turbulence models. *Int. J. for Numer. Methods in Fluids*, 1994, **19**, 939.
18. Xia, J. L., Smith, B. L., Benim, A. C., Schmidli, J. and Yadigaroglu, G., Influence of boundary conditions on swirling flow in combustors. *FED*, 1996, **237**, 789.
19. Imao, S. and Itoh, M., Turbulent characteristics of the flow in an axially rotating pipe. *Int. J. Heat and Fluid Flow*, 1996, **17**, 444.
20. Clarke, D. S. and Wilkes, N. S., The calculation of turbulent flows in complex geometries using a differential stress model. AERE-R13428, 1989.
21. AEA Technology, CFX Release 4.1, User Guide, Harwell, 1996.
22. Leonard, B. P., A stable and accurate convective modelling procedure based on quadratic upstream interpolation. *Methods in Applied Mech. Eng.*, 1979, **19**, 59.
23. Van Doormal, J. P. and Raithby, G. D., Enhancements of the SIMPLE method for predicting incompressible fluid flows. *Numer. Heat Transfer*, 1984, **7**, 147.
24. Xia, J. L., Benim, A. C., Smith, B. L., Schmidli, J. and Yadigaroglu, G., Effect of three dimensionality on swirling flows with/without combustion. *National Heat Transfer Conference*. Baltimore, Maryland, 10–12 August 1997.